A&A 466, 1065–1076 (2007)
DOI: 10.1051/0004-6361:20066742

Astronomy & Astrophysics

Interferometric multi-wavelength (sub)millimeter continuum study of the young high-mass protocluster IRAS 05358+3543⋆

H. Beuther[1], S. Leurini[2,3], P. Schilke[2], F. Wyrowski, K. M. Menten[2], and Q. Zhang[4]

[1] Max-Planck-Institute for Astronomy, Königstuhl 17, 69117 Heidelberg, Germany
e-mail: beuther@mpia.de
[2] Max-Planck-Institute for Radioastronomy, Auf dem Hügel 69, 53121 Bonn, Germany
e-mail: name@mpifr-bonn.mpg.de
[3] European Southern Observatory, Karl-Schwarzschild-Str. 2, 85748 Garching, Germany
e-mail: sleurini@eso.org
[4] Harvard-Smithsonian Center for Astrophysics, 60 Garden Street, Cambridge, MA 02138, USA
e-mail: qzhang@cfa.harvard.edu

Received 14 November 2006 / Accepted 9 February 2007

ABSTRACT

Aims. We study the small-scale structure of massive star-forming regions through interferometric observations in several (sub)mm wavelength bands. These observations resolve multiple sources, yield mass and column density estimates, and give information about the density profiles as well as the dust and temperature properties.
Methods. We observed the young massive star-forming region IRAS 05358+3543 at high spatial resolution in the continuum emission at 3.1 and 1.2 mm with the Plateau de Bure Interferometer, and at 875 and 438 μm with the Submillimeter Array. The observations are accompanied by VLA 3.6 cm archival continuum data.
Results. We resolve at least four continuum sub-sources that are likely of protostellar nature. Two of them are potentially part of a proto-binary system with a projected separation of 1700 AU. Additional (sub)mm continuum peaks are not necessarily harboring protostars but maybe caused by the multiple molecular outflows. The spectral energy distributions (SEDs) of the sub-sources show several features. The main power house mm1, which is associated with CH_3OH maser emission, a hypercompact HII region and a mid-infrared source, exhibits a typical SED with a free-free emission component at cm and long mm wavelengths and a cold dust component in the (sub)mm part of the spectrum (spectral index between 1.2 mm and 438 μm $\alpha \sim 3.6$). The free-free emission corresponds to a Lyman continuum flux of an embedded 13 $M_\odot$ B1 star. The coldest source of the region, mm3, has $\alpha \sim 3.7$ between 1.2 mm and 875 μm, but has lower than expected fluxes in the shorter wavelength 438 μm band. This turnover of the Planck-function sets an upper limit on the dust temperature of mm3 of approximately 20 K. The uv-data analysis of the density structure of individual sub-cores reveals distributions with power-law indices between 1.5 and 2. This resembles the density distributions of the larger-scale cluster-forming clump as well as those from typical low-mass cores.

Key words. stars: formation – stars: early-type – stars: individual: IRAS 05358+3543 – ISM: dust, extinction – ISM: jets and outflows

1. Introduction

Single-dish (sub)mm continuum imaging in high-mass star-forming regions revealed various interesting properties of the dust and gas clumps harboring the star-forming clusters. The derived physical parameters include the gas masses, the gas column densities, the spectral indices and resulting dust properties as well as the density distributions of the gas on cluster scales (Hatchell et al. 2000; van der Tak et al. 2000; Molinari et al. 2000; Mueller et al. 2002; Beuther et al. 2002b; Hatchell & van der Tak 2003; Walsh et al. 2003; Williams et al. 2004; Fontani et al. 2005; Williams et al. 2005; Hill et al. 2005; Klein et al. 2005; Faúndez et al. 2004; Beltrán et al. 2006). However, all these studies had insufficient spatial resolution (at best 16 000 AU at 2 kpc distance) to resolve sub-structure within the star-forming regions, and thus were inadequate to study the properties of individual cluster members or unresolved multiple systems. A further limitation was that many of such studies only covered one frequency band (870 μm or 1.2 mm) and hence could not investigate the spectral index of the gas emission, which allows to set constraints on the dust properties.

To overcome some of these limitations we conducted a comprehensive program observing the very young massive star-forming region IRAS 05358+3543 at high spatial resolution with the Submillimeter Array (SMA[1]) in the 438 and 875 μm band, and with the IRAM Plateau de Bure Interferometer (PdBI[2]) in the 1.2 and 3.1 mm bands. These observations resolve the high-mass star-forming cluster into various sub-components at four different wavelengths, allowing to study the physical properties of individual cluster members or still unresolved, likely gravitationally bound multiple systems in great detail.

⋆ Data corresponding to Figs. 2–4, and 6 are available in electronic form at the CDS via anonymous ftp to
cdsarc.u-strasbg.fr (130.79.128.5) or via
http://cdsweb.u-strasbg.fr/cgi-bin/qcat?J/A+A/466/1065

[1] The Submillimeter Array is a joint project between the Smithsonian Astrophysical Observatory and the Academia Sinica Institute of Astronomy and Astrophysics, and is funded by the Smithsonian Institution and the Academia Sinica.
[2] IRAM is supported by INSU/CNRS (France), MPG (Germany), and IGN(Spain).

IRAS 05358+3543 is part of a sample of 69 High-Mass Protostellar Objects (HMPOs) investigated in depth over the last few years by Sridharan et al. (2002); Beuther et al. (2002b–d); Williams et al. (2004, 2005); Fuller et al. (2005). At a kinematic distance of 1.8 kpc, the bolometric luminosity of the region is $10^{3.8}\,L_{\odot}$, and the integrated gas mass is $\sim$300 $M_{\odot}$[3]. H_2O and Class II CH_3OH maser emission was studied at high spatial resolution (Tofani et al. 1995; Minier et al. 2000; Beuther et al. 2002d), but so far no cm continuum emission had been detected down to the threshold of 1 mJy, indicative of the very young evolutionary stage of the region. Furthermore, high-spatial-resolution interferometric observations of the region revealed at least three molecular outflows, one of them being the most collimated massive molecular outflow known today (Beuther et al. 2002a). These observations also resolved the evolving protocluster at 2.6 mm wavelength with a $4'' \times 3''$ beam into three sub-sources (mm1 to mm3) with gas masses between 37 and 50 $M_{\odot}$[3]. Figure 1 gives an overview of the large and small-scale dust continuum emission from previous observations (Beuther et al. 2002b,a). Two of the three identified outflows emanate from the vicinity of mm1. McCaughrean et al. (in prep.) detected with Keck observations two mid-infrared sources in the region, one being spatially coincident with the main mm continuum peak mm1. This mid-infrared source was recently resolved by Longmore et al. (2006) into a double-source separated by $1''$ corresponding to 1800 AU. Near-infrared polarimetric imaging also revealed a deeply embedded source associated with mm1 (Yao et al. 2000). Previously identified infrared sources, some of them were suggested to be the outflow driving sources (Porras et al. 2000), were shown to be offset from the main mm and mid-infrared sources and hence unlikely to be the main power houses in the region (Beuther et al. 2002a).

In this paper, we present the (sub)mm continuum observations from all four wavelengths bands. The corresponding spectral line data will be published separately by Leurini et al. (in prep.). For the nomenclature of this paper, we use the term protostar (and corresponding proto-cluster, proto-binary) for massive young stellar objects that are still actively accreting, independent of whether they have started hydrogen burning already or not.

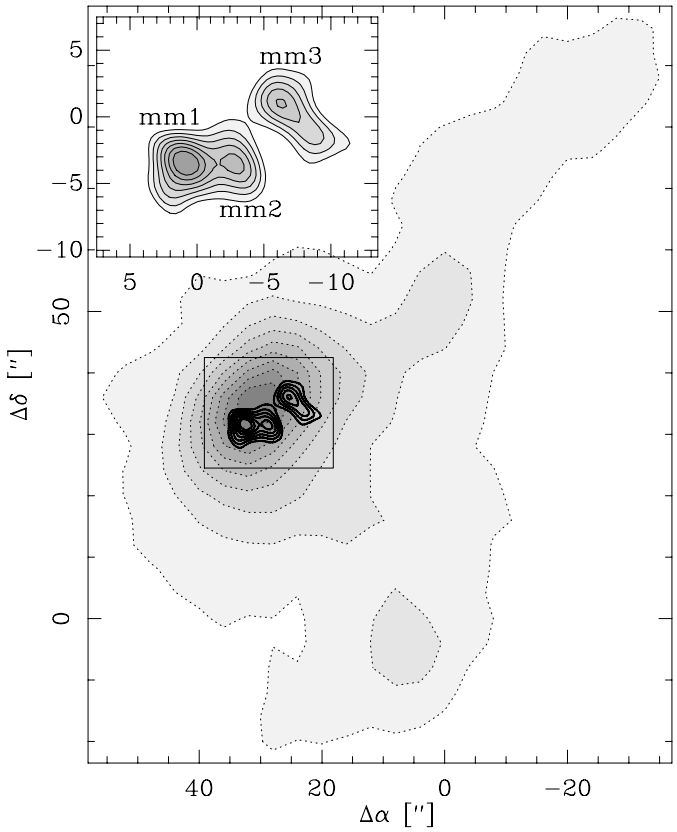

Fig. 1. Overview of the region. The large emission shown in grey-scale with dotted contours is the 1.2 mm continuum emission observed with the MAMBO array at the IRAM 30 m telescope (Beuther et al. 2002b). The full contours (enlarged in the inlay-box) show the 2.6 mm continuum data from the PdBI at a spatial resolution of $4.0'' \times 3.0''$ with the labeled three identified mm continuum sources (Beuther et al. 2002a). The 1.2 mm MAMBO data are contoured from 106 mJy beam^{-1} to 954 mJy beam^{-1} (step 106 mJy beam^{-1}), the 2.6 mm PdBI are contoured from 6.6 mJy beam^{-1} to 22.0 mJy beam^{-1} (step 2.2 mJy beam^{-1}). The (0/0) position of the large map is the position of the IRAS 05358+3543 source which is derived from the IRAS 12 μm image, whereas the mm continuum peak correlates with the IRAS 100 μm peak. The (0/0) position of the inlay is the phase center of the older observations by Beuther et al. (2002a).

2. Observations and data reduction

We observed IRAS 05358+3543 with three interferometers (SMA, PdBI and VLA) in ten different configurations or spectral setups. The most important observational parameters are given in Table 1. The velocity of rest was $v_{\rm lsr} = -17.6\,{\rm km\,s^{-1}}$, and the flux accuracy of the observations is estimated to be good within 20%. Below we discuss a few additional details of the different observations.

2.1. Submillimeter array observations at 875 μm

The SMA observations in the compact and extended configuration were centered at 348/338 GHz (upper and lower sideband, USB/LSB, 875 μm). The projected baselines ranged between 15 and 252 kλ. The short baseline cutoff implies that source structures $\geq 16''$ are filtered out by the observations. The phase center of the observations was RA(J2000.0) $05^{\rm h}39^{\rm m}13\overset{\rm s}{.}07$ and Dec(J2000.0) $+35^{\circ}45'51\overset{''}{.}2$. The zenith opacities, measured with the NRAO tipping radiometer located at the Caltech Submillimeter Observatory, were good during both tracks with τ(348GHz) $\sim$ 0.18 (scaled from the 225 GHz measurement via τ(348GHz) $\sim 2.8 \times \tau$(225GHz)). The correlator had a bandwidth of 1.968 GHz and the channel separation was 0.8125 MHz. Measured double-sideband system temperatures corrected to the top of the atmosphere were between 150 and 500 K, mainly depending on the elevation of the source. The initial flagging and calibration was done with the IDL superset MIR originally developed for the Owens Valley Radio Observatory (Scoville et al. 1993) and adapted for the SMA[4]. The imaging and data analysis was conducted in MIRIAD (Sault et al. 1995). During the observations on November 11th, 2004, the position of the primary calibrator 3C111 was wrong in the catalog by $\sim 0.6''$. Therefore, we self-calibrated our secondary phase calibrator 0552+398 (16.3° from the source) shifting it in the map to the correct position. The solutions were then applied to IRAS 05358+3543. The 875 μm continuum data were produced by averaging the apparently line-free part of the USB and LSB data. The corresponding line

[3] The cited gas masses are at a 50% level of the masses originally presented in Beuther et al. (2002b,a) because of different assumptions for the dust opacities (Beuther et al. 2005).

[4] The MIR cookbook by Charlie Qi can be found at `http://cfa-www.harvard.edu/~cqi/mircook.html`.

Table 1. Main observation parameters.

λ	Obs	Date	Config.	Calibrators			Θ	1σ
				Phase/Amp.	Flux dens.	Bandpass		
(mm)							($''$)	$\left(\frac{\mathrm{mJy}}{\mathrm{beam}}\right)$
36	VLA	08/02-06/03	AB	0555+398	3C 286	0555+398	0.49×0.41	0.018
3.1	PdBI	01/03-10/03	BCD	0528+134	NRAO150	0420-014	$1.9 \times 1.4''$	0.3
				552+398	0528+134	3C 454.2		
						NRAO150		
1.2	PdBI	01/03-10/03	BCD	0528+134	NRAO150	0420-014	1.26×0.84	2.3
				0552+398	0528+134	3C 454.2		
						NRAO150		
1.2	PdBI	02/05	AB	0529+483	3C 273	3C 84	0.6×0.44	1.4
				J0418+380	3C 273			
0.875	SMA	11/04	comp.	3C111	Callisto	Jupiter	1.14×0.57	7
						& Callisto		
0.875	SMA	01/05	ext.	3C111	Callisto	Jupiter	1.14×0.57	7
					3C 279	3C 279		
0.438	SMA	01/06	comp.	Vesta	Callisto	Callisto	1.4×0.9	400
						& Uranus		

The table shows the observing frequency λ, the observatories, the dates of observation, the array configurations, the calibrators, the resulting synthesized beam Θ and the 1σ value of the final maps.

emission will be discussed in a separate paper by Leurini et al. (in prep.).

2.2. Submillimeter array observations at 438 μm

The weather conditions for the 438 μm/690 GHz observations were excellent with a zenith opacity τ(230 GHz) between 0.03 and 0.05 throughout the night. This corresponds to zenith opacities at 690 GHz between 0.6 and 1.0 (τ(690 GHz) $\sim 20 \times$ (τ(230 GHz) $-$ 0.01), Masson 1994). The phase center and correlator setup were the same as for the 875 μm observations. The primary beam of the SMA at these high frequencies is $\sim$18$''$. The covered frequency ranges were 679.78 to 681.75 GHz and 689.78 to 691.75 GHz. Measured double-sideband system temperatures corrected to the top of the atmosphere were between 1350 and 10 000 K, depending on the elevation of the source and the opacity. The sensitivity was limited by the strong side-lobes of the strongest emission peaks. Since the third main mm continuum source is approximately at the edge of the SMA primary beam at this frequency, we applied a correction for the primary beam attenuation to the final image to determine the fluxes more properly. Although the synthesized beam of the continuum image is $1.4'' \times 0.9''$, we work only on a smoothed version with a $1.9'' \times 1.4''$ beam, comparable to the 3 mm data.

2.3. Plateau de bure interferometer observations at 1.2 and 3.1 mm

The PdBI was used in two different frequency setups in 2003 and 2005. A first frequency setup was performed in four tracks between January and October 2003 in the B-C and D configurations of the array. The reference center is RA (J2000) $05^{\mathrm{h}}39^{\mathrm{m}}13\overset{\mathrm{s}}{.}0$ and Dec(J2000) $35^{\circ}45'54\overset{''}{.}$. The 3 mm receivers were used in single sideband mode and tuned to 96.6 GHz; the 1 mm receivers, in double sideband mode, were tuned to 241.85 GHz, (USB). One 320 MHz unit was placed to obtain a continuum measurement at 3.1 mm. Four overlapping 160 MHz units were used to obtain the 1.2 mm continuum measurement. The system temperatures varied between 100 and 150 K in the 3.1 mm band, and between 300 and 600 K in the 1.2 mm band. The second frequency setup was observed in 2005 in the A and B configurations. The 1 mm receivers were tuned in lower sideband to 241.2 GHz. Three 160 MHz units were used to get the continuum measurement. Measured system temperatures in the 1.2 mm receivers ranged between 240 and 1000 K, with one receiver measuring system temperatures of 900 K. The data calibration were performed in CLIC, and the imaging in MAPPING, both packages are part of the GILDAS software suite[5].

2.4. Very large array archival data at 3.6 cm

Searching the Archive of the Very Large Array (VLA), we found A+B array data observed at 3.6 cm wavelength in 2002 and 2003 (project AR482). The data were reduced with the standard AIPS procedures.

3. Results

3.1. Small-scale dust/gas distribution

The high-spatial-resolution multi-frequency data allow to disentangle considerable sub-structure in this massive young star-forming cluster. Figure 2 presents overlays of the 1.2 mm and the 875 μm dust continuum emission. The top-panel shows images at both wavelengths with comparable resolution (BCD configuration with the PdBI at 1.2 mm, and extended+compact configuration with the SMA at 875 μm). The 3.1 mm and 438 μm images with slightly lower spatial resolution will be discussed below (Sect. 3.2). We clearly resolve many sub-features compared to the more simple three sources previously detected at lower spatial resolution (see Fig. 1 and Beuther et al. 2002a). Furthermore, we have additional 1.2 mm continuum data with even higher spatial resolution ($0.6'' \times 0.4''$, AB configuration with the PdBI) shown in the bottom-panel of Fig. 2. While this highest-spatial-resolution dataset filters out nearly all large-scale emission it clearly identifies the most compact sources. We could have combined all four configurations, but since the most extended configurations dominate this image, we refrained from that.

[5] See `http://www.iram.fr/IRAMFR/GILDAS`

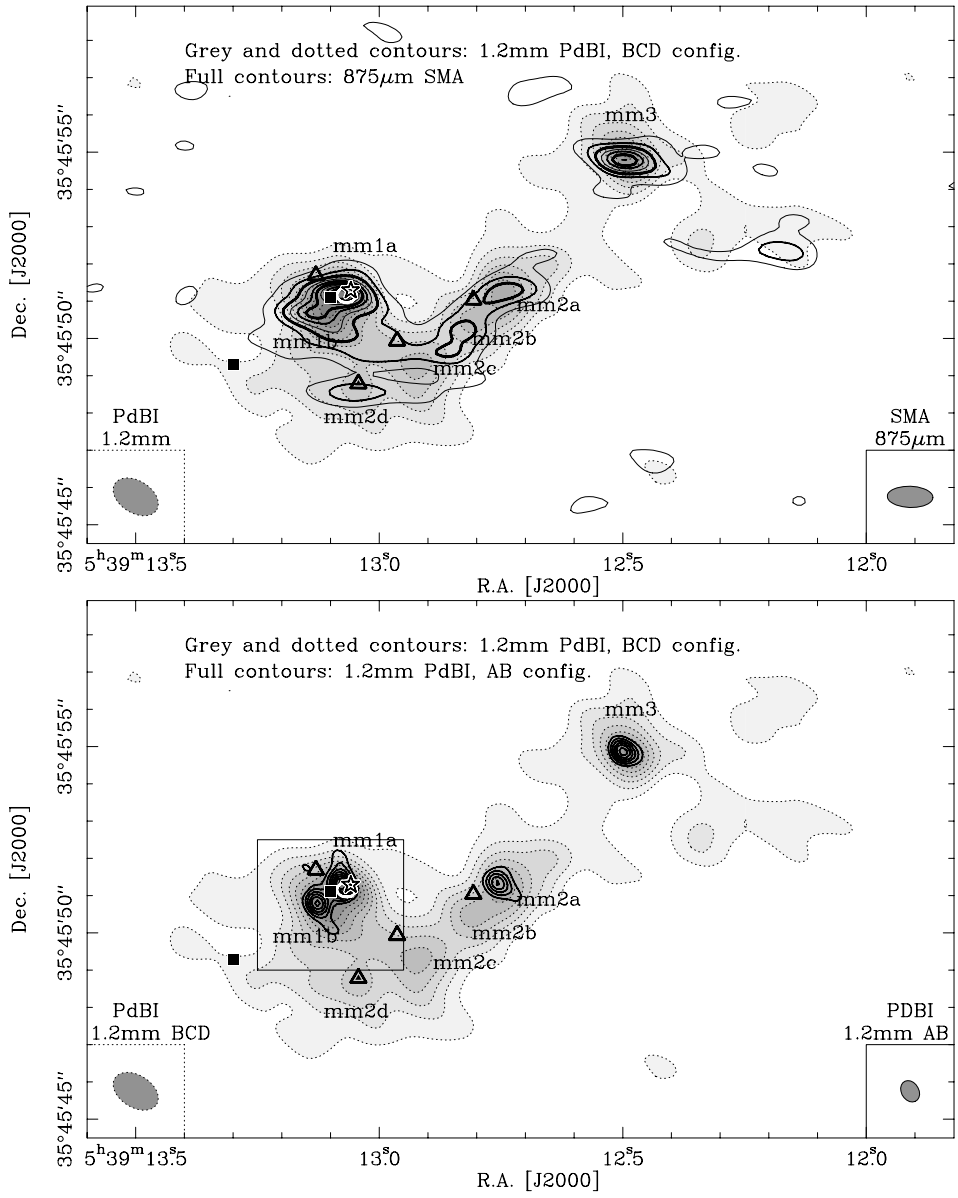

Fig. 2. (Sub)mm continuum images toward IRAS 05358+3543 at 1.2 mm (PdBI) and at 875 μm (SMA). The top panel shows in grey-scale with dotted contours the 1.2 mm data (BCD configuration) and in full contours with increasing thickness the 875 μm data. The contouring is done from 10 to 90% of the peak emission of each image (step 10%), with peak flux values of 58.9 and 164.3 mJy beam^{-1} for the 1.2 mm and 875 μm bands, respectively. The bottom-panel shows in grey-scale with dotted contours again the same 1.2 mm data (BCD configuration), and in full contours the 1.2 mm data observed at even higher spatial resolution ($0.6'' \times 0.4''$) in the AB configuration. The contouring of the latter dataset is from 20 to 90% (step 10%) of the peak flux 29.8 mJy beam^{-1}. In both panels, the white ellipse shows the VLA 3.6 cm 50% contour level (0.31 mJy). The star, triangles and squares mark the positions of the Class II CH_3OH maser (Minier et al. 2000), the H_2O masers (open triangles from Tofani et al. 1995 and small filled triangle from Beuther et al. 2002d) and the mid-infrared sources (McCaughrean et al. in prep.). The newly identified double-source mm1a and mm1b is labeled as well. The box outlines the region shown in Fig. 3. The files for this figure are also available in electronic form at the CDS.

The main (sub)mm continuum source mm1, which is at the center of two molecular outflows (Beuther et al. 2002a), is resolved into two separate (sub)mm continuum peaks, mm1a and mm1b. This is already observable at $\sim 1''$ in Fig. 2 (top panel) but more clearly discernable in the highest-resolution data in the bottom panel of Fig. 2 and the zoom in Fig. 3. The compact 3.6 cm continuum source and the Class II CH_3OH maser are associated with mm1a. The cm continuum source is unresolved at the given spatial resolution with a peak flux of 0.62 mJy beam^{-1} (below the detection limit of 1 mJy by Sridharan et al. 2002), and we only show the 50% contour level in Figs. 2 & 3. The closest H_2O maser feature detected by Tofani et al. (1995) is $\sim 1''$ north-east of mm1a and not clearly associated with one or the other peak as well. It should be noted that this feature was not detected by Beuther et al. (2002d), probably due to variability of the feature. The projected separation between mm1a and mm1b amounts to $\sim 0.94''$, corresponding to a projected linear separation of $\sim$1700 AU at the given distance (1.8 kpc). The main mid-infrared source detected by Longmore et al. (2006) coincides well with the position of mm1a (Fig. 3). However, while the secondary source mm1b is $\sim$1700 AU toward the south-east, the secondary mid-infrared source is $\sim$1800 AU south-west of

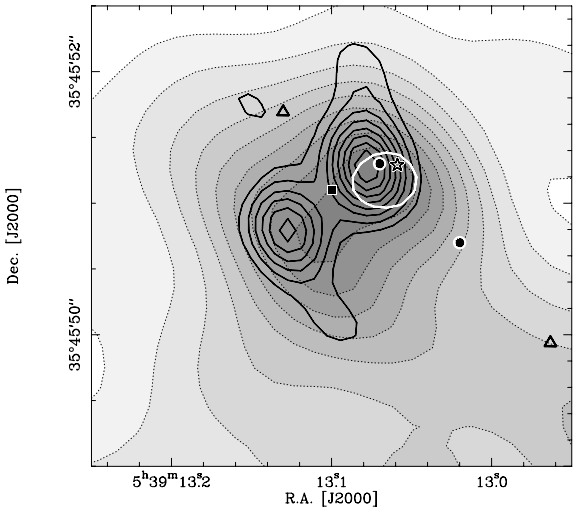

Fig. 3. Zoom into the central region of mm1a and mm1b as shown in Figure 2. The grey-scale with dotted contours shows again the same 1.2 mm data (BCD configuration), and in full contours the 1.2 mm data observed at higher spatial resolution ($0.6'' \times 0.4''$) in the AB configuration. The contouring is the same as in Fig. 2. The white ellipse shows the VLA 3.6 cm 50% contour level (0.31 mJy). The star, triangles and squares mark the positions of the Class II CH_3OH maser (Minier et al. 2000), the H_2O masers (Tofani et al. 1995) and the mid-infrared sources (McCaughrean et al. in prep.). The black-and-white circles show the double mid-infrared sources discussed by Longmore et al. (2006). The 0.5″ positional difference between the main mid-infrared peak positions by McCaughrean et al. and Longmore et al. can be accounted for by relatively poor pointing accuracies and the difficulties of registering mid-infrared data. The files for this figure are also available in electronic form at the CDS.

mm1a. Hence, mm1b and the secondary mid-infrared source are apparently independent indicating even more sub-structure in the evolving young cluster.

The previously identified source mm2 is resolved even more, at least into two sub-sources mm2a and mm2b (Fig. 2). However, while mm2a shows the same peak position in the 1.2 mm band and the 875 μm band, the peaks associated with mm2b are separated by approximately 0.4″. The mm peak mm2c is identified in the 1.2 mm image but not at shorter wavelengths. Inspecting the longer wavelength 3.1 mm data in Fig. 4, one finds an elongation in this lower-spatial-resolution dataset toward the mm2c position as well (labeled "jet?" in Fig. 4). Since also the spectral index between the 1.2 mm and 875 μm toward this position is very low (of the order 1.5, see Sect. 3.4 and corresponding Fig. 6) this feature may be due to an underlying outflow/jet. The feature mm2d in Fig. 2 is again discernable in both bands. One of the H_2O maser features by Tofani et al. (1995) is associated with this latter (sub)mm continuum emission feature.

The third source mm3 remains a single compact object even at the highest spatial resolution. The lower-resolution 3.1 mm image in Fig. 1 (inlay) shows an elongation from mm3 toward the south-west, and the higher-resolution images in Fig. 2 show weak emission there as well. Since these weak emission features show different peak positions in the 1.2 mm and the 875 μm bands, we refrain from further discussion of this feature.

Protostellar condensations should be detectable in all (sub)mm wavelengths bands and not be filtered out in very extended configurations. Therefore, we identify at ∼0.5″ spatial resolution (∼900 AU) four compact protostellar sources in the region (mm1a, mm1b, mm2a, mm3) , the positions are listed in Table 2.

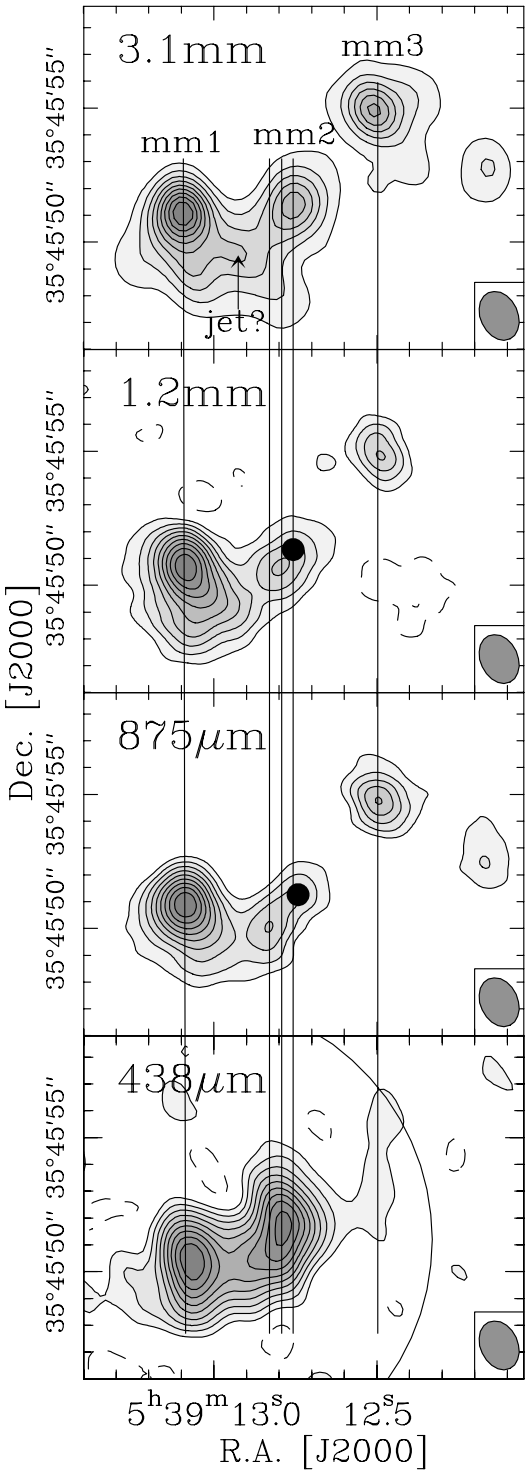

Fig. 4. (Sub)mm continuum images in the four observed bands smoothed to the spatial resolution of $1.9'' \times 1.4''$ of the lowest resolution image at 3.1 mm. The contour levels are from 10 to 90% (step 10%) of the peak emissions with peak fluxes of 10.3, 91.8, 270.8, and 3569 mJy beam^{-1} for the 3.1 mm, 1.2 mm, 875, and 438 μm bands, respectively. The 438 μm image shown here is not primary-beam corrected yet, the size of the primary beam is indicated by the large half-circle in the bottom panel. The left and right vertical lines mark the positions of mm1 and mm3. In contrast, the peak position of mm2 shifts with wavelengths in these lower-resolution images which is indicated by the three middle vertical lines. However, the full circles mark the mm2a peak position in the corresponding high-resolution images (Fig. 2). The files for this figure are also available in electronic form at the CDS.

Table 2. Positions of the four identified protostellar sources.

Source	RA [J2000]	Dec [J2000]
mm1a	05:39:13.08	35:45:51.3
mm1b	05:39:13.13	35:45:50.8
mm2a	05:39:12.76	35:45:51.3
mm3	05:39:12.50	35:45:54.9

3.2. The multi wavelength dataset

Since our 3.1 mm data are of lower spatial resolution, we can smooth the higher frequency data to this resolution ($1.9'' \times 1.4''$) and investigate the SEDs of the relatively larger subcomponents. Fig. 4 presents the compilation of all four continuum images at the spatial resolution of the 3.1 mm continuum dataset. We clearly identify three (sub)mm continuum peaks at all wavelengths, the formerly known sources mm1 to mm3. The vertical lines in Fig. 4 locate the RA positions in the three lower-frequency bands (3.1 mm, 1.2 mm and 875 μm). While the positions of mm1 and mm3 coincide very well between the different bands, the position of mm2 shifts progressively toward the south-east going from 3.1 mm to 875 μm. However, comparing the 1.2 mm and 875 μm lower-resolution images in Fig. 4 with the higher-spatial-resolution images presented in Fig. 2, we see that the source mm2 consists of at least two sub-sources, mm2a and mm2b. While the 1.2 mm and 875 μm positions of mm2a coincide well (Fig. 2 and filled circles in Fig. 4), the peak position of mm2b is shifted toward the south-east going from 1.2 mm to the 875 μm data. Based on the lower-resolution 3.1 mm image, it appears likely that at higher spatial resolution mm2b would be even closer to mm2a going to even longer wavelengths. This positional shift of mm2b as well as the non-detection of mm2c in the 875 μm indicates that the dust emission at these positions is not of typical protostellar nature, but caused by other processes, e.g., the protostellar outflows in the region. As already mentioned in Sect. 3.1, the 3.1 mm image exhibits a smaller peak between mm1 and mm2 which is approximately associated with mm2c in the shorter-wavelength higher-resolution data (Fig. 2). Taking additionally into account the low spectral index toward this position (see below), this feature is likely produced by an underlying jet/outflow (Reynolds 1986), hence we labeled it the jet-feature in the 3.1 mm image.

The 438 μm image requires some additional explanations because interferometric imaging at these frequency is still exploratory and very difficult. The sub-source mm1 is at the phase center and the most reliable feature. The emission peak of mm2 does not shift further to the south-east as maybe expected from the lower-frequency data, but the RA position coincides approximately with the 1.2 mm peak position whereas the Declination position is even closer to the 3.1 mm position. Furthermore, the emission around mm2 in this band extends a little bit further to the north than in the other images. We are not entirely certain whether this is an artifact of the comparably lower data quality in this band, or whether it may even be real because many of the molecular line maps (e.g., CH_3OH, H_2CS or $C^{34}S$) have an additional emission peak north of mm2 as well (Leurini et al. in prep.). Since high-spatial-resolution images at these wavelengths are extremely rare so far (only 2 are published to our knowledge, Orion-KL by Beuther et al. 2006 and TW Hydra by Qi et al. 2006), it is hard to set additional constraints here. The location of mm3 is right at the edge of the primary beam of our dataset (the phase center was chosen like that because we were also interested in the CO(6–5) emission from the main outflow emanating from mm1), and the measured fluxes toward mm3 are barely above the noise ($\sim 2.5\sigma$). To at least derive an upper limit for the emission from mm3, we corrected the image shown in Fig. 4 for the primary beam attenuation. The derived fluxes shown in Table 3 and used below for the mass/column density estimates, and spectral energy distributions are measured from the primary-beam-corrected image.

Table 3. (Sub)mm continuum fluxes and derived masses/column densities.

Source	$S_{\rm int.}$ [mJy]	$S_{\rm Peak}$ $\left[\frac{\rm mJy}{\rm beam}\right]$	M^e [$M_\odot$]	$N^e_{\rm H_2}$ [cm^{-2}]
3.1 mm (AB) with $1.9'' \times 1.4''$ beam				
mm1	20	10.3	10.6	1.7×10^{24}
mm2	10	5.9	5.3	9.7×10^{23}
mm3[d]	13	6.5	18.5	2.9×10^{24}
1.2 mm (BCD) with $1.9'' \times 1.4''$ beam				
mm1	215	91.8	5.0	6.6×10^{23}
mm2	64	38.3	1.5	2.7×10^{23}
mm3[d]	39	37.6	2.7	8.1×10^{23}
875 μm with $1.9'' \times 1.4''$ beam				
mm1	529	270.8	3.8	6.0×10^{23}
mm2	199	110.1	1.4	2.4×10^{23}
mm3[d]	165	137.5	3.9	1.0×10^{24}
438 μm with $1.9'' \times 1.4''$ beam[b]				
mm1	8630	3589	6.5	8.4×10^{23}
mm2	11450	3749	8.6	8.8×10^{23}
mm3[c,d]	941	941	3.2	9.9×10^{23}
1.2 mm (AB) with $0.60'' \times 0.44''$ beam				
mm1a	42	29.8	1.0	2.2×10^{24}
mm1b	26	22.3	0.6	1.6×10^{24}
mm2a	31	18.3	0.7	1.3×10^{24}
mm3[d]	27	22.8	1.9	4.9×10^{24}
1.2 mm (BCD) with $1.26'' \times 0.84''$ beam				
mm1a	67	58.9		1.1×10^{24}
mm1b	62	54.8		9.8×10^{23}
mm2a	67	39.9		7.2×10^{23}
mm2b	33	33.3		6.0×10^{23}
mm2c	65	32.1		5.8×10^{23}
mm2d	41	26.5		4.8×10^{23}
mm3[d]	103	48.0		2.6×10^{24}
875 μm with $1.14'' \times 0.57''$ beam				
mm1a	225	164.3		1.5×10^{24}
mm1b	124	106.4		9.6×10^{23}
mm2a	97	62.5		5.7×10^{23}
mm2b	69	58.6		5.3×10^{23}
mm2c	?[a]			
mm2d	68	46.2		4.2×10^{23}
mm3[d]	212	116.1		3.5×10^{24}

[a] No clear emission peak in that band. [b] Fluxes in this band are measured from the primary-beam corrected image. [c] The flux values are only 2.5σ. [d] A colder temperature of 20 K was used for mm3 (Sect. 3.4). [e] The masses and column densities are estimated to be accurate within a factor 4.

3.3. Mass and column density estimates

Assuming that the (sub)mm continuum emission is optically thin and thus tracing the whole dust column densities with a gas to dust mass ratio of 100, we can derive the gas column densities $N_{\rm H_2}$ and gas masses M following Hildebrand (1983) and Beuther et al. (2002b). The following sections will discuss the spectral indices toward the various sub-regions in IRAS 05358+3543 in

more detail, but for the mass calculations we adopt a dust opacity index β of 1.5, corresponding to dust opacities κ of 0.2, 0.9, 1.4, and 4.0 $\mathrm{cm^2\,g^{-1}}$ at 3100, 1200, 875, and 438 μm, respectively. Although the region contains gas components at various temperatures (see Leurini et al. in prep.), we assume an average temperature of 50 K for the mass estimates. Only for mm3, we use a lower temperature of 20 K as derived from the spectral energy distribution shown in Sect. 3.4. Given the uncertainties of the dust opacities and the temperatures, we estimate the masses and column densities to be accurate within a factor 4. Table 3 presents the derived masses for the various sub-sources estimated from the multi-wavelength dataset.

As expected, the derived masses are all below the previous single-dish 1.2 mm and lower-resolution 3 mm PdBI mass estimates (Sect. 1). Some part of the discrepancy can be solved by the different assumption for the dust opacity β used in the previous studies ($\beta = 2$, Beuther et al. 2002b,a) and here ($\beta = 1.5$). However, the difference in β accounts to a mass difference of approximately a factor 2 at 1.2 mm and 875 μm, and the larger effect is the missing flux in the new interferometer data. The integrated single-dish fluxes at 1.2 mm and 850 μm are 6 Jy and 28.7 Jy (Williams et al. 2004), respectively, whereas the integrated fluxes in our high-spatial-resolution 1.2 mm (BCD configuration) and 875 μm images (Fig. 2) are 0.85 Jy and 1.37 Jy, respectively. Thus, we are recovering only between 15% and 5% of the flux – and hence mass – in these interferometric images. The difference in flux recovery can already be recognized by just comparing the values for the 1.2 mm data in the AB and BCD configurations, respectively (Table 3). Therefore, we omit the mass estimates of the higher-resolution data in Table 3.

An additional effect arises from the various wavelength observations: Comparing the three mass estimates derived from 3.1 mm, 1.2 mm and 875 μm data with the same spatial resolution ($1.9'' \times 1.4''$, Table 3), the masses at 1.2 mm and 875 μm are approximately the same, whereas the masses obtained from the 3.1 mm data are more than a factor 2 higher. We will discuss the spectral energy distributions in detail below, but already this comparison indicates that at 3 mm additional non-dust contributions to the continuum flux have to be taken into account.

Regarding the flux measurements and mass/column density estimates in the 438 μm band, the values for mm1 are reasonable compared to the other bands. Since the 438 μm flux for mm3 is only 2.5σ limit, the derived mass and column density can be considered as an upper limit. The strangest values are for mm2 in the 438 μm band because they are higher than for mm1 whereas this is always the other way round in the longer wavelength bands. As discussed in the previous section, with the current data is is difficult to decide whether this is an artifact of the dataset, or whether there are additional contributions to the continuum emission in this band as maybe suggested by the strong line emission peaks a small distance to the north of mm2 (Leurini et al. in prep.).

3.4. Spectral energy analysis from the multi-wavelength (sub)mm continuum images

In spite of the complexity of the region, we can derive the SEDs from the lower-resolution images toward mm1, mm2 and mm3 (Fig. 4). The emission in the 3.1 mm and 438 μm bands appears a little more extended which may be due to a better sampling of the uv-plane at the corresponding scales. Therefore, we refrain from using integrated fluxes for the various positions but rather use the peak fluxes listed in Table 3. The peak fluxes are derived at the peak position of each image. Figure 5 presents the final (sub)mm SEDs for the three positions at the given spatial resolution.

For all three (sub)mm peaks mm1 to mm3, the 3.1 mm point is consistently too high to be fitted with a single power law which is expected for pure dust continuum emission at (sub)mm wavelength. Therefore, the (sub)mm power-law fits at all three positions were derived from the shorter wavelength data only.

Source mm1: the 1.2 mm to 438 μm data are well fitted by a single power-law $S \propto \nu^{\alpha}$ with $\alpha \sim 3.6 \pm 0.3$. This power-law exponent corresponds in the Rayleigh-Jeans regime to a dust opacity index $\beta = \alpha - 2$ of 1.6 ± 0.3, observed often in high- and low-mass star-forming regions (e.g., Andre et al. 2000; Beuther et al. 2007). The low-frequency 8.3 GHz data from the VLA are likely from a hypercompact HII region. Therefore, we can fit the whole spectrum from 3.6 cm to 438 μm with a uniform density hypercompact HII region at low to intermediate frequencies and a dust component in the short mm to submm range (Fig. 5 top-left panel). This is a typical spectrum one expects from a young massive protostar where the central source has already started hydrogen burning. Following Rohlfs & Wilson (2006), we can calculate the emission measure (EM) using the approximate turnover frequency of 35 GHz and en electron temperature of $\sim 10^4$ K. The derived EM of $\sim 5.4 \times 10^9$ $\mathrm{cm^{-6}}$ pc is very high, about one to two orders of magnitude higher than values found in typical ultracompact HII regions (e.g., Kurtz et al. 1994). Taking the optical thin free-free flux of ~6.4 mJy at 60 GHz (Fig. 5) and following Kurtz et al. (1994), we calculate a Lyman continuum flux of $\sim 10^{45.4}$ photons $\mathrm{s^{-1}}$, which corresponds approximately to a B1 Zero-Age-Main-Sequence star with a luminosity of $\sim 10^{3.72}\,L_{\odot}$ and a stellar mass of $\sim 13\,M_{\odot}$ (Panagia 1973; Lang 1992). Based on the strong, collimated outflow that emanates from the vicinity of mm1 with an outflow rate of $6 \times 10^4\,M_{\odot}$ and a dynamical timescale of 3.6×10^4 yrs (Beuther et al. 2002a), it is likely that this source is still in its accretion process, and therefore, we still call it a protostar. The luminosity derived from the free-free emission is of the same order as the total luminosity ($\sim 10^{3.8}\,L_{\odot}$) derived from the IRAS data (Sridharan et al. 2002), indicating that the luminosity of the whole region is really dominated by the most massive protostar.

Source mm3: we can fit the 1.2 mm and 875 μm data reasonably well with a power-law with $\alpha \sim 3.7 \pm 0.3$ (corresponding to $\beta \sim 1.7 \pm 0.3$). The 3.1 mm fluxes are too high for that fit. Taking our 8.3 GHz VLA 3σ upper limits of 56 μJy, it is again possible to fit the low-frequency part of the spectrum with a hypercompact HII (Fig. 5 bottom-left panel). A point of caution here is that the turnover frequency from the optically thick to the optically thin regime is relatively high, between 70 and 100 GHz. One possible way to explain this is that the region is so young that the forming HCHII region is still quenched and thus optically thick up to relatively high frequencies without having the time and power to heat the surrounding gas. Of particular interest is the high-frequency data-point at 438 μm which is below the expectation of the power-law fit from the 1.2 mm and 875 μm. Since we have no cm nor compact line detection toward mm3 (see Beuther et al. 2002a and Leurini et al. in prep.), this sub-source is a potential candidate for a still very cold massive core at even earlier evolutionary stages. For such a cold core, the peak of the SED moves to longer wavelength and one does not expect a normal Rayleigh-Jeans-like power-law at short submm wavelengths anymore. Therefore we tried to fit the high-frequency SED with grey-body functions with varying temperature (blackbody functions modified by $1 - \mathrm{e}^{\tau_\nu}$ taking into account the finite optical depth τ_ν of the dust at all frequencies). The two bottom-panels in Fig. 5 show such grey-body functions with temperatures

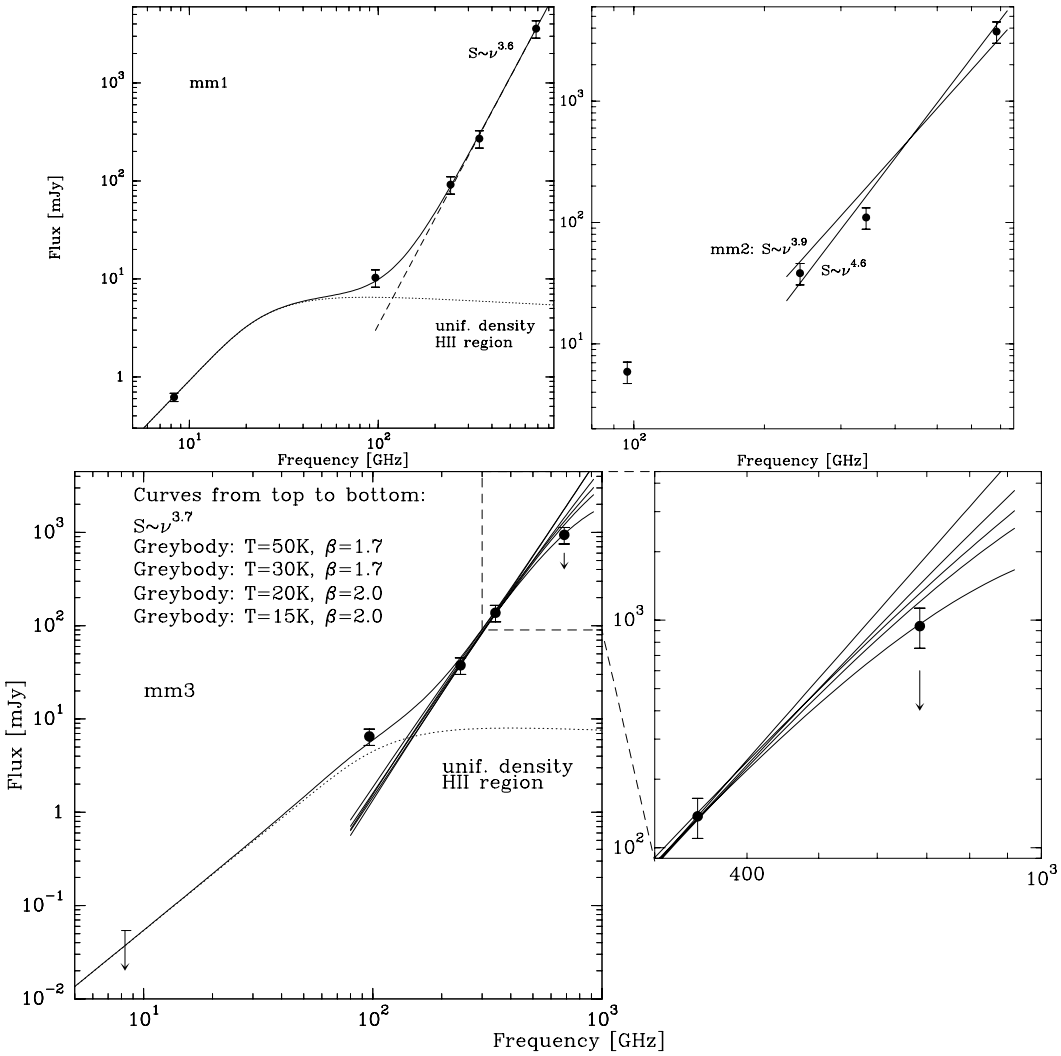

Fig. 5. Spectral energy distributions (SEDs) for mm1, mm2 and mm3. For mm1 and mm3, the data are fitted with a uniform density HII region at low frequencies and a power-law with exponent 3.6 and 3.7 in the (sub)mm part of the spectrum, respectively. For mm3, we present also various grey-body functions varying the temperature T and the dust emissivity index β as labeled in the plot. The arrows in the mm3 SEDs mark the upper limits (1σ noise at 8.3 GHz, and the tentative 941 mJy detection corresponding to 2.5σ at 685 GHz). For mm2, we show two extreme power-laws fitting the 1.2 mm and the 438 μm but missing the 865 μm point. We measured the fluxes toward the peak positions of each image in Fig. 4, respectively.

between 50 and 15 K (we also varied β between 1.7 and 2). One has to keep in mind that mm3 is at the edge of the primary beam, that the imaging is difficult and that the data are primary-beam corrected. Nevertheless, these grey-body functions indicate that most of the envelope dust and gas is likely at $\leq$20 K.

Source mm2: as already mentioned in the previous sections, mm2 is the strangest of the three sources. We do not find any reasonable fit for the 1.2 mm to 438 μm. The fits presented in Fig. 5 (top-right panel) show the extreme power-laws fitting the 1.2 mm and the 438 μm data. The 875 μm data point is below these fits. As pointed out previously, it may be possible that the unproportionally high 438 μm flux density could be partly an artifact of this dataset. However, there may also be additional contributions in this band (e.g., from the adjacent molecular line peak) which have to be taken into account separately. Furthermore, the data used for these SEDs are of lower spatial resolution smearing out mm2a and mm2b. Since mm2b may be caused by an outflow/jet with a lower spectral index (see the following paragraphs), this will likely increase the complication of interpreting mm2's SED (see also the cases of L1157 or IRAS 20293+3952, Gueth et al. 2003; Beuther et al. 2004). In principal, a flattening of the SED in the long wavelength regime could also be produced by a change of the dust grain size distribution towards larger fractions of large grains within a protostellar disk. However, this appears an unlikely scenario here because a low spectral index is also observed in the larger-scale envelope of the region (Williams et al. 2004). Based on these data and the complicated structure of the region, we are not able to draw further conclusions from the SED of mm2.

To derive additional small-scale information about the (sub)mm dust continuum emission, we used the higher-spatial-resolution 1.2 mm and 875 μm data to produce a spectral index map of the (sub)mm continuum emission. Therefore, we restored both datasets with the same synthesized beam of $1.2'' \times 0.8''$. To account for absolute positional differences due to non-perfect phase calibration, we shifted the 875 μm image by $0.18''$ to the east aligning the peak-positions of mm1a and mm3. Then the ratio map was constructed from these two images (Fig. 6). The spatial distributions of the two restored maps shown in the top-panel of Fig. 6 show that the spatial scales traced in both bands are approximately the same, and thus a comparison of both images appears reasonable. Taking into account the flux uncertainties of

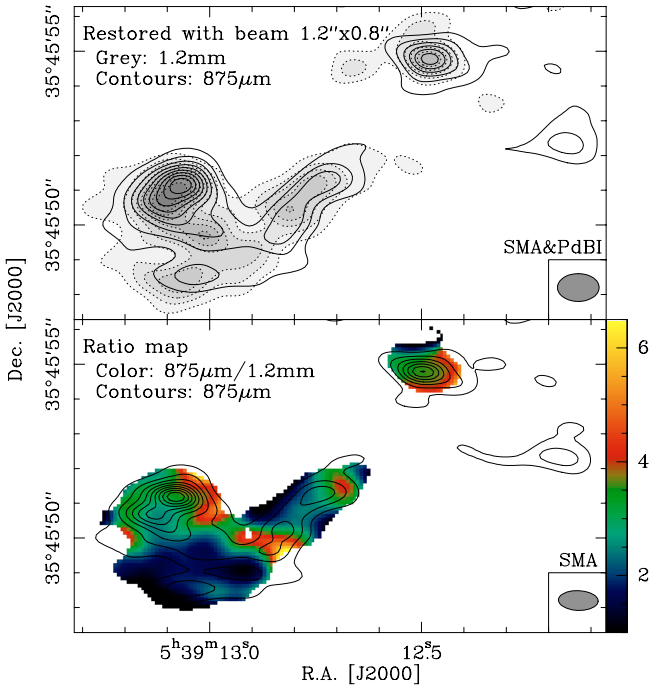

Fig. 6. Ratio map of the 875 μm versus the 1.2 mm data. Both datasets were smoothed to a common spatial resolution of $1.2'' \times 0.8''$. To better align the two maps before producing the ratio, the 875 μm was shifted by $0.18''$ to the west. The top panel shows the two maps at the same spatial resolution. The bottom panel then presents the ratio map in color scale with the 875 μm data at original resolution overlayed in contours. The synthesized beam of the data used for the ratio map is shown at the bottom-right of the top panel, and the bottom-right of the bottom panel shows the synthesized beam of the 875 μm map at original resolution.The files for this figure are also available in electronic form at the CDS.

20%, the different uv-sampling and the positional shift, we estimate the uncertainties of this spectral index map of the order ±0.5. Edge effects of rising spectral index toward the north-west of mm1a or toward the south-east of mm1b are most likely an artifact. Similarly, the contrast of a low spectral index north of mm3 and a high spectral index south of mm3 are potential artifacts caused by the division of the different datasets. However, the variations of the spectral indices throughout the region which are not edge effects are likely to be real.

The spectral indices we derive from Fig. 6 toward the four protostellar condensations mm1a, mm1b, mm2a, and mm3 (Table 2) are 3.6, 2.7, 2.3, and 3.6, respectively. The spectral indices toward mm1a and mm3 – approximately the same as in the lower-resolution data discussed before – correspond to a rather normal dust opacity index β of 1.6 (e.g., Draine 2006), whereas the spectral indices toward mm1b and mm2a are significantly lower. Since we aligned the two wavelength images simultaneously with the peak positions from mm1a and mm3, the lower values toward the other sources are likely to be real and no artifact from the shifting. The positional shifting of mm2b from 1.2 mm to 875 μm (Fig. 2) is reflected in the ratio gradient toward that region. Since mm2c is not detected at 875 μm at all, the corresponding spectral index is hence very low (of the order 1.5) indicative of an underlying jet (Reynolds 1986). Another interesting position appears to be west of mm2a, where particularly high values >4 are found in the ratio map. Figure 6 clearly demonstrates the complexity of spectral index studies and the large spread in spectral indices over very small spatial regions. Possible physical implications will be discussed in Sect. 4.2.

Table 4. Results of power-law fits to the continuum amplitudes versus uv-distances of the embedded protostellar sources.

	mm1a[a]	mm2	mm3
α(3.1mm)	–0.59	–0.78	–0.61
α(1.2mm)	–0.86	–0.71	–0.53
α(875μm)	–0.93	–1.05	–0.94
α av.	-0.8 ± 0.2	-0.85 ± 0.2	-0.7 ± 0.2
p(3.1mm)	2.0	1.8	2.0
p(1.2mm)	1.7	1.9	2.1
p(875μm)	1.7	1.5	1.7
p av.[b]	1.8 ± 0.3	1.75 ± 0.3	1.9 ± 0.3

[a] The fit was centered on mm1a but it covers mainly structures combining mm1a and mm1b. [b] The error for the average p takes also into a account an error for q of ±0.2.

3.5. Radial structure analysis from the multi-wavelength (sub)mm continuum uv-data

To investigate the structure of the protostellar sub-sources detected in the continuum, the data were analyzed directly in the uv-domain avoiding the uv-sampling and cleaning difficulties. To decrease the influence of the other sub-sources on the analysis of a particular object, two-dimensional Gaussians were fit as a first approximation to the highest resolution images and the corresponding models were removed from the uv-data, resulting in "clean" uv-datasets for each of the three main sub-sources. Then the data for each sub-source were binned in uv-annuli around the peak positions and averaged vectorially. The averaged amplitudes versus uv-radius are shown for the 3 sources at the 3 observed wavelengths in Fig. 7. Toward mm1, we selected the the mm1a peak position as the center, but obviously most baselines trace structures combining mm1a and mm1b, and only the largest baselines (≥250 kλ) are only due to mm1a. Therefore, the derived intensity and density profile is for the multiple system mm1a/mm1b. Most of the data can be fit reasonably well by straight lines in the log-log plots, showing that the radial structures of the sources are close to power-law profiles. The data are inconsistent with Gaussians sources. Some of the data show evidence for constant amplitudes at the largest uv-radii, hinting at point source components at the smallest scales. Deviations from the straight lines are due to more complicated morphology imprinted on power-law profiles, e.g. the substructures in mm1 and mm2.

Table 4 shows the results of the power-law fits to the data. Assuming that the emission is due to dust at all frequencies, the radial profiles should be the same at different frequencies. The differences that can be seen in the data therefore shows the observational limitations of this method of radial profile analysis. Looney et al. (2003) give a relation between the power-law profiles in the image and uv-planes, as well as how the observed uv-power-law indices $V(s)$ are composed by the density and temperature structure: $V(s) \sim s^{p+q-3}$, where p and q are the power-law indices of the density $n \sim r^{-p}$ and temperature structure $T \sim r^{-q}$, respectively. With a typical temperature power-law index of 0.4, density indices from 1.5 to 2.0 translate to –1.1 to –0.6 in the uv plane. Inspecting the observed values in Table 4 shows that the millimeter cores have density profiles in this range.

4. Discussion

4.1. Protostellar powerhouses and other sources

The double-structure mm1a and mm1b is separated by only ~1700 AU projected on the plane of the sky. This double-system

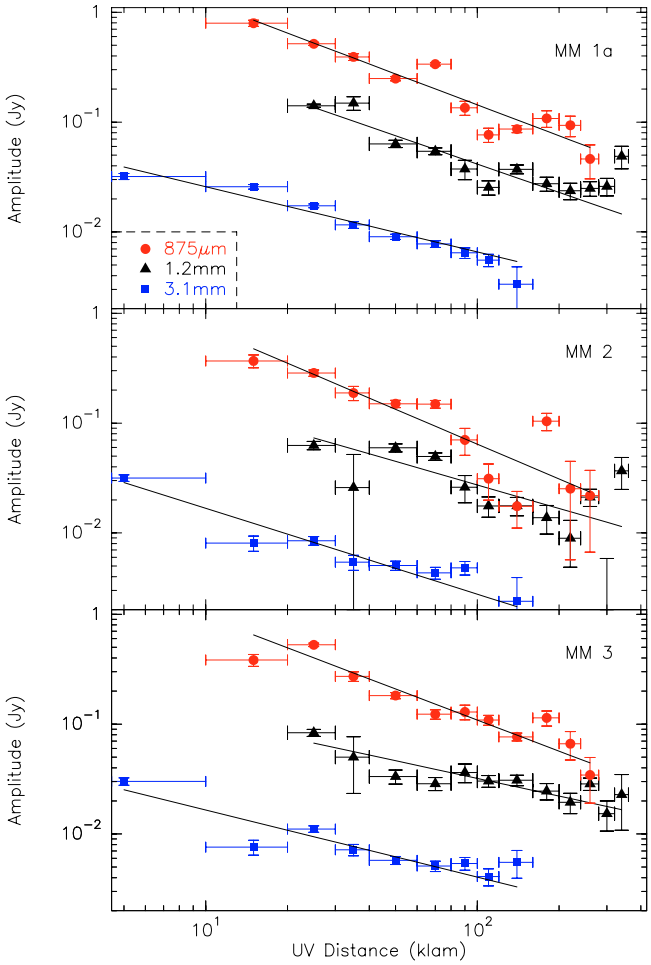

Fig. 7. Plots of amplitude versus uv-distance for the three main sub-sources in IRAS 05358+3543 at three observed frequencies. Results from power-law fits are shown as well. Although the top panel was produced centered on mm1a, the data ≤250 kλ are from scales combining mm1a and mm1b. Therefore it resembles the intensity and density structure of this multiple system.

may well be a massive bound binary system, similar to the potential high-mass protocluster or binary system W3(H_2O) (Wyrowski et al. 1999; Chen et al. 2006). Considering also the third source detected at mid-infrared wavelengths by Longmore et al. (2006), there may be three sources within a projected circle with radius of ∼1000 AU. To carry the analogy with the W3 region even further, we note that the ultracompact HII region/molecular hot core W3(OH) lies at a similar distance from W3(H_2O) (Wyrowski et al. 1999) as IRAS 05358+3543 mm2 and mm3 from mm1a/b. The measured expansion age of the W3(OH) UCHII region is only 2300 years (Kawamura & Masson 1998). It is well possible that IRAS 05358+3543 which now harbors a hypercompact HII region might evolve in to an UCHII region on a similar time scale, whereas mm2 and mm3 might evolve into regions resembling the present mm1a/b [and W3(H_2O)] on similar time scales.

The two sources mm1a/b are located within one apparently common gas and dust core, and the projected separation of ∼1700 AU is within the range of observed distances for proto-binary sources (Launhardt 2004). From the molecular line data presented in Leurini et al. (in prep.) we are not able to derive a clear velocity structure around the two cores which could be attributed to common rotation (e.g., Launhardt 2004). However, since we know about the complexity of the region and two molecular outflows emanating from the common mm1 core, it is not even a surprise that a coherent velocity signature is missing. Each sub-source, mm1a and mm1b, could drive one of two molecular outflows detected by Beuther et al. (2002a). Based on the higher flux of mm1a (Table 3), its association with the compact cm continuum source, the Class II CH_3OH maser and the main mid-infrared source, mm1a is the main power-house of the region likely driving the more energetic large-scale collimated north-south outflow.

Interestingly, of the four mm2 sub-sources, only mm2a is detected as a compact source in the highest resolution 1.2 mm image. This is indicative of mm2a being a genuine protostellar source whereas the emission features associated with mm2b, mm2c and mm2d could be more transient structures maybe caused by the underlying multiple outflow system.

The source mm3 appears as the most simple object in the IRAS 05358+3543 massive star-forming region since it remains a single peak and shows a spectral index indicative of protostellar dust emission. The turnover of the SED at the shortest submm wavelengths indicates that mm3 is the coldest sub-source in this region. Hence, mm3 is a likely the youngest detected protostar in this system and may potentially drive one of the multiple outflows identified in the region.

While the CH_3OH Class II maser can clearly be associated with mm1a, none of the four H_2O masers can be associated with any of the protostellar sources. Since H_2O masers are believed to be produced in shock fronts they do not necessarily have to be located in close proximity to protostellar sources.

4.2. Dust evolution and spectral indices

While dust opacity indices β of 2 are usually found in the interstellar medium, lower values are possible in star-forming cores. For example, the dust opacity per unit dust mass κ(1.3mm) ∼ 0.9 $cm^2\,g^{-1}$ suggested by Ossenkopf & Henning (1994) for grains with thin ice mantles at gas densities of $10^6\,cm^{-3}$ corresponds to $\beta \sim 1.4$. Similarly, grain growth and dust coagulation in dense molecular cores decreases the values for β as well (e.g., Beckwith et al. 2000; Draine 2006). A note of caution has to be added that the effect of a low spectral index α can also be caused by high optical depth from an underlying accretion disk and/or hypercompact HII region, which can mimic low values of β. Although it is difficult to differentiate between both scenarios, many studies favor the grain-growth scenario.

The values β of 1.6 and 1.7 measured toward mm1 and mm3 from the lower-resolution dataset indicate that in these sub-sources the dust has probably not evolved much yet and the dust properties are still close to their properties in the interstellar medium. The SED of mm2 is too complex to derive a reasonable dust opacity index from the given dataset.

The picture gets even more complicated going to the higher-spatial-resolution ratio map presented in Fig. 6. Similar to the lower-resolution data, two of the protostellar objects (mm1a and mm3) exhibit a rather normal spectral index of 3.6, corresponding to a dust opacity index β of 1.6. While the spectral index of 2.7 for mm1b is already lower, it still is consistent with grain growth or high optical depth scenarios.

Although the very low value of $\alpha \sim 2.3$ toward the mm2a peak would still be consistent with grain growth in circumstellar disks or very high optical depths, the fact that we see a similarly low spectral index on larger spatial scales (Williams et al. 2004) indicates that additional physical processes may also come into play. Since we know of at least three molecular outflows emanating from the region, these outflows/jets are the most likely

culprits to change the observed spectral indices. Thermal ionized wind models predict spectral indices between 2 and −0.1 with typical spherical winds exhibiting spectral indices $\alpha \sim 0.6$ (Reynolds 1986). Since these winds turn optically thin going to higher frequencies, their contribution to the SED is relatively larger at longer wavelength. Therefore, adding a wind component on top of the expected dust emission, a flattening of the spectral index is possible. Spectral indices below 2 as observed toward mm2c and its surroundings can be due solely to the outflows within the region (see also Reynolds 1986).

Even more puzzling are the large spectral indices >4 found in the vicinity of mm2b and north-west of mm2a. Similarly high spectral indices were observed toward the outflow region within the L1157 low-mass star-forming region by Gueth et al. (2003) as well as toward some parts of the Orion molecular ridge and a cold molecular cloud near the Galactic Center (Lis et al. 1998; Lis & Menten 1998). While Gueth et al. (2003) attribute these high spectral indices to potentially smaller dust grains and/or chemical properties (e.g., Kruegel & Siebenmorgen 1994; Pollack et al. 1994), Lis et al. (1998) and Lis & Menten (1998) find that their high-β locations are at low temperatures. Therefore, they suggest that the high β values can be caused by dust grains covered with thick ice mantles (see also Aannestad 1975). This picture is confirmed by recent modeling of the dust opacity by Boudet et al. (2005) indicating that β decreases with increasing temperature, and that β can be as high as 2.5 (corresponding to a spectral index $\alpha = 4.5$) at temperatures of 15 K. However, it is not obvious that the temperatures toward the high-alpha positions in Fig. 6 should be particularly low, and thus it is questionable whether this picture can explain our observations. The fact that the positions of mm2b do not coincide between the 1.2 mm and the 875 μm bands also indicates that dynamic processes like protostellar outflows can significantly alter the (sub)mm continuum emission.

It is also interesting to compare the spectral indices we get at high spatial resolution with previous spectral index studies of the whole region with single-dish SCUBA observations at the JCMT. Williams et al. (2004) derive a mean spectral index of 2 increasing toward the (sub)mm peak to 2.6. This value is still significantly lower than the 3.6 we measure toward mm1 which is the position of the single-dish peak. Obviously, the single-dish data measure only some kind of weighted average of the values one resolves with interferometric observations.

4.3. Density structure of massive star-forming cores

The radial structure of the IRAS 05358+3543 dust continuum on large spatial scales probed by bolometer arrays has been studied by Beuther et al. (2002b) and Williams et al. (2005). These observations resulted in radial density profiles of the cluster-forming gas and dust clump with power-law distributions of $p = 1.9$ and 1.5 for the 1.2 mm and 850 μm data, respectively. It is interesting that we find approximately the same power-law distributions in the uv-analysis of the individual subsources. Hence, the density structure of the large-scale cluster-forming clump appears to be similar to the small-scale structure of its fragmented star-forming sub-cores. Furthermore, the density distributions we find for the massive star-forming cores resemble those derived previously for low-mass star-forming regions (e.g., Motte & André 2001). The only other high-mass study we know of that analyzed the structure of massive star-forming cores with sub-arcsec resolution is by Chen et al. (2006) towards W3(H_2O) where they found density indices again close to 1.5. These results are consistent with the analytic models and hydrodynamic simulations of massive cores by McKee & Tan (2003) and Krumholz et al. (2007).

4.4. Limitations and future prospects

Although these observations are among the highest-spatial-resolution multi-wavelength studies existing today, there are obviously still limitations to what we can resolve. The finest spatial resolution of ∼0.5″ we achieve at 1.2 mm corresponds at the given distance of 1800 pc to a linear resolution of 900 AU, and we know from young objects like W3IRS5 (e.g., Megeath et al. 2005) to more evolved regions like Orion (e.g., Preibisch et al. 1999) that multiplicity at scales <1000 AU can well be present. Köhler et al. (2006) recently reported binary fractions for the Orion cluster of 23 ± 10% for stars >2 $M_\odot$ and 3.6 ± 3.2% for stars <2 $M_\odot$. Even in IRAS 05358+3543 we resolve mm1 into a double-system (or triple system if including the MIR data) with spatial separations of ∼1700 AU (Sect. 4.1). Therefore, all parameters we derive for the various (sub)mm sub-sources have to be considered as potentially harboring multiple objects. This is particularly important for the data at lower resolution (>1″), where we know that they do not even resolve mm1a and mm1b properly. For example, as mentioned in Sect. 3.5, the radial density profile derived toward the peak position of mm1a is actually the density structure from the envelope encompassing mm1a and mm1b. Similar arguments hold for the SED analysis and the mass and column density estimates.

Nevertheless, it is likely that the expected multiple unresolved sub-sources are gravitationally bound and that they form from the same gas and dust reservoir. Therefore, mass, column density, temperature and density distribution of such entities are still the relevant parameters for the physical properties of the collapsing cores. This is consistent with recent 3D hydrodynamically simulations showing that collapsing cores fragment less than previously expected, and that the most massive fragments are likely forming within the massive accretion disk (Krumholz et al. 2007) which we do not resolve here anyway.

The only way to observationally assess the fragmentation of young and cold massive star-forming cores in more detail is with higher spatial resolution and higher sensitivity. While the spatial resolution of the SMA and PdBI reaches today at best ∼0.3″ (less than a factor 2 better than the presented observations), the brightness sensitivity for these instruments at such scales is relatively poor. However, in only a few years from now, the Atacama Large Millimeter Array (ALMA) will be able to work regularly at 0.1″ scales with good enough sensitivity to detect even lower-mass members of the evolving protoclusters. Then we will be able to derive the small scale-fragmentation processes in better detail than possible today.

5. Summary

We have observed the very young massive star-forming region IRAS 05358+3543 interferometrically with high spatial resolution in four frequency bands between 3.1 mm and 438 μm wavelength with the Plateau de Bure Interferometer and the Submillimeter Array. The observations reveal at least four subsources at the center of the region that are likely of protostellar nature. One of them, mm1a, is associated with CH_3OH Class II maser emission, a cm wavelength hypercompact HII region and a mid-infrared source. The center of two molecular outflows – one of them the most collimated massive molecular outflow observed so far in high-mass star formation – splits up

into a double-source (mm1a and mm1b) with a projected separation of 1700 AU. With the given data, we cannot distinguish whether this projected double-source is really a proto-binary system or whether they are unbound. The additionally detected mid-infrared source ∼1800 AU south-west of mm1a indicates a relatively high protostellar density with at least three protostars in a projected circle with radius of ∼1000 AU. The main power house of the region is the sub-source mm1a, but the other sub-sources are likely to power outflows as well. Furthermore, we detect additional (sub)mm peaks (mm2b, mm2c and mm2d) which may not necessarily be of protostellar nature but which could be caused by the underlying outflows and jets. H_2O maser emission is found within the region of dust continuum emission but no feature is clearly associated with a protostellar (sub)mm continuum peak. This indicates that H_2O maser emission is likely be produced in outflow shock fronts.

This multi-frequency high-spatial-resolution (sub)mm continuum dataset allows for the first time a spectral index analysis of individual sub-sources in a massive evolving cluster that contain either individual protostars or unresolved, likely gravitationally bound multiple systems. The spectral energy distribution of the main power house mm1 resembles a typical SED one expects for a massive star-forming core: a hypercompact HII region from a 13 $M_\odot$ B1 star is detected at cm wavelength whereas the mm to submm spectrum is dominated by a cold dust component with a spectral index of 3.6. The 438 μm data are of particular interest because they fit well into the dust spectrum derived previously from the longer wavelength data. The SED of the sub-source mm3 shows a different behavior at this short wavelength: although we can only derive upper limits at 438 μm for mm3, this upper limit is significantly below the power-law spectrum that one can fit from the lower-frequency data and that would be expected for a normal Rayleigh-Jeans-like part of the SED. Such a lower flux measurement can be explained by even colder dust emission where the peak of the SED shifts to longer wavelength and hence the 438 μm point is already closer to this peak and thus not on the Rayleigh-Jeans tail of the Planck-function anymore. Trying various grey-body functions, we estimate an upper limit for the dust temperature of 20 K.

A radial analysis of the data in the uv-domain reveals that the density power-law indices p vary for the different sub-sources between 1.5 and 2, similar to observed density distributions of low-mass star-forming cores. Furthermore, these power-law indices resemble those previously found for the larger-scale cluster-forming clump, indicative of similar density distributions on the high-mass star- and cluster-forming scale.

Although the discussed sub-sources may still harbor multiple objects, the derived physical parameters should represent the properties of individual collapsing massive cores well. Fragmentation on even smaller spatial scales (e.g., within the massive accretion disks) will likely only be observationally accessible with the advent of ALMA in a few years from now.

Acknowledgements. We thank the PIs of the VLA cm-wavelength project AR482 Luis Rodriguez and Bo Reipurth for having no objections against us using these data. We are also thankful to Jan Martin Winters and Roberto Neri for their support during the reduction of the PdBI data. Furthermore, we acknowledge the referee's and the editor's reports that helped clarifying this paper. H.B. acknowledges financial support by the Emmy-Noether-Program of the Deutsche Forschungsgemeinschaft (DFG, grant BE2578).

References

Aannestad, P. A. 1975, ApJ, 200, 30
Andre, P., Ward-Thompson, D., & Barsony, M. 2000, Protostars and Planets IV, 59
Beckwith, S. V. W., Henning, T., & Nakagawa, Y. 2000, Protostars and Planets IV, 533
Beltrán, M. T., Brand, J., Cesaroni, R., et al. 2006, A&A, 447, 221
Beuther, H., Schilke, P., Gueth, F., et al. 2002a, A&A, 387, 931
Beuther, H., Schilke, P., Menten, K. M., et al. 2002b, ApJ, 566, 945
Beuther, H., Schilke, P., Sridharan, T. K., et al. 2002c, A&A, 383, 892
Beuther, H., Walsh, A., Schilke, P., et al. 2002d, A&A, 390, 289
Beuther, H., Schilke, P., & Wyrowski, F. 2004, ApJ, 615, 832
Beuther, H., Schilke, P., Menten, K. M., et al. 2005, ApJ, 633, 535
Beuther, H., Zhang, Q., Reid, M. J., et al. 2006, ApJ, 636, 323
Beuther, H., Churchwell, E. B., McKee, C. F., & Tan, J. C. 2007, in Protostars and Planets V, ed. B. Reipurth, D. Jewitt, & K. Keil, 165
Boudet, N., Mutschke, H., Nayral, C., et al. 2005, ApJ, 633, 272
Chen, H.-R., Welch, W. J., Wilner, D. J., & Sutton, E. C. 2006, ApJ, 639, 975
Draine, B. 2006, ApJ, 636, 1114
Faúndez, S., Bronfman, L., Garay, G., et al. 2004, A&A, 426, 97
Fontani, F., Beltrán, M. T., Brand, J., et al. 2005, A&A, 432, 921
Fuller, G. A., Williams, S. J., & Sridharan, T. K. 2005, A&A, 442, 949
Gueth, F., Bachiller, R., & Tafalla, M. 2003, A&A, 401, L5
Hatchell, J., & van der Tak, F. F. S. 2003, A&A, 409, 589
Hatchell, J., Fuller, G. A., Millar, T. J., Thompson, M. A., & Macdonald, G. H. 2000, A&A, 357, 637
Hildebrand, R. H. 1983, QJRAS, 24, 267
Hill, T., Burton, M. G., Minier, V., et al. 2005, MNRAS, 363, 405
Kawamura, J. H., & Masson, C. R. 1998, ApJ, 509, 270
Klein, R., Posselt, B., Schreyer, K., Forbrich, J., & Henning, T. 2005, ApJS, 161, 361
Köhler, R., Petr-Gotzens, M. G., McCaughrean, M. J., et al. 2006, A&A, 458, 461
Kruegel, E., & Siebenmorgen, R. 1994, A&A, 288, 929
Krumholz, M., Klein, R., & McKee, C. 2007, ApJ, 656, 959
Kurtz, S., Churchwell, E., & Wood, D. O. S. 1994, ApJS, 91, 659
Lang, K. R. 1992, Astrophysical Data I, Planets and Stars, X, 937 pp. 33 figs. (Berlin, Heidelberg, New York: Springer-Verlag)
Launhardt, R. 2004, in IAU Symp., 213
Lis, D. C., & Menten, K. M. 1998, ApJ, 507, 794
Lis, D. C., Serabyn, E., Keene, J., et al. 1998, ApJ, 509, 299
Longmore, S. N., Burton, M. G., Minier, V., & Walsh, A. J. 2006, MNRAS, 369, 1196
Looney, L. W., Mundy, L. G., & Welch, W. J. 2003, ApJ, 592, 255
Masson, C. R. 1994, in ASP Conf. Ser., 87
McKee, C. F., & Tan, J. C. 2003, ApJ, 585, 850
Megeath, S. T., Wilson, T. L., & Corbin, M. R. 2005, ApJ, 622, L141
Minier, V., Booth, R. S., & Conway, J. E. 2000, A&A, 362, 1093
Molinari, S., Brand, J., Cesaroni, R., & Palla, F. 2000, A&A, 355, 617
Motte, F., & André, P. 2001, A&A, 365, 440
Mueller, K. E., Shirley, Y. L., Evans, N. J., & Jacobson, H. R. 2002, ApJS, 143, 469
Ossenkopf, V., & Henning, T. 1994, A&A, 291, 943
Panagia, N. 1973, AJ, 78, 929
Pollack, J. B., Hollenbach, D., Beckwith, S., et al. 1994, ApJ, 421, 615
Porras, A., Cruz-González, I., & Salas, L. 2000, A&A, 361, 660
Preibisch, T., Balega, Y., Hofmann, K.-H., Weigelt, G., & Zinnecker, H. 1999, New Astron., 4, 531
Qi, C., Wilner, D. J., Calvet, N., et al. 2006, ApJ, 636, L157
Reynolds, S. P. 1986, ApJ, 304, 713
Rohlfs, K., & Wilson, T. L. 2006, Tools of radio astronomy, 4th rev. and enl. ed. K. Rohlfs, & T. L. Wilson (Berlin: Springer)
Sault, R. J., Teuben, P. J., & Wright, M. C. H. 1995, in Astronomical Data Analysis Software and Systems IV, ASP Conf. Ser. 77, 433
Scoville, N. Z., Carlstrom, J. E., Chandler, C. J., et al. 1993, PASP, 105, 1482
Sridharan, T. K., Beuther, H., Schilke, P., Menten, K. M., & Wyrowski, F. 2002, ApJ, 566, 931
Tofani, G., Felli, M., Taylor, G. B., & Hunter, T. R. 1995, A&AS, 112, 299
van der Tak, F. F. S., van Dishoeck, E. F., & Caselli, P. 2000, A&A, 361, 327
Walsh, A. J., Macdonald, G. H., Alvey, N. D. S., Burton, M. G., & Lee, J.-K. 2003, A&A, 410, 597
Williams, S. J., Fuller, G. A., & Sridharan, T. K. 2004, A&A, 417, 115
Williams, S. J., Fuller, G. A., & Sridharan, T. K. 2005, A&A, 434, 257
Wyrowski, F., Schilke, P., Walmsley, C. M., & Menten, K. M. 1999, ApJ, 514, L43
Yao, Y., Ishii, M., Nagata, T., Nakaya, H., & Sato, S. 2000, ApJ, 542, 392